Large-Eddy Simulation of Deep-Cycle Turbulence in an Equatorial Undercurrent Model

HIEU T. PHAM, SUTANU SARKAR, AND KRAIG B. WINTERS

*Department of Mechanical and Aerospace Engineering, and Scripps Institution of Oceanography,
University of California, San Diego, La Jolla, California*

ABSTRACT

Dynamical processes leading to deep-cycle turbulence in the Equatorial Undercurrent (EUC) are investigated using a high-resolution large-eddy simulation (LES) model. Components of the model include a background flow similar to the observed EUC, a steady westward wind stress, and a diurnal surface buoyancy flux. An LES of a 3-night period shows the presence of narrowband isopycnal oscillations near the local buoyancy frequency N as well as nightly bursts of deep-cycle turbulence at depths well below the surface mixed layer, the two phenomena that have been widely noted in observations. The deep cycle of turbulence is initiated when the surface heating in the evening relaxes, allowing a region with enhanced shear and a gradient Richardson number Ri_g less than 0.2 to form below the surface mixed layer. The region with enhanced shear moves downward into the EUC and is accompanied by shear instabilities and bursts of turbulence. The dissipation rate during the turbulence bursts is elevated by up to three orders of magnitude. Each burst is preceded by westward-propagating oscillations having a frequency of 0.004–0.005 Hz and a wavelength of 314–960 m. The Ri_g that was marginally stable in this region decreases to less than 0.2 prior to the bursts. A downward turbulent flux of momentum increases the shear at depth and reduces Ri_g. Evolution of the deep-cycle turbulence includes Kelvin–Helmholtz-like billows as well as vortices that penetrate downward and are stretched by the EUC shear.

1. Introduction

Turbulent mixing in the Equatorial Undercurrents (EUC) system has been the focus of many field observations such as Tropic Heat I (Gregg et al. 1985), Tropic Heat 2 (Moum et al. 1992; McPhaden and Peters 1992), Tropical Instability Wave Experiment (Lien et al. 1996), and recent campaigns in 2002 (Lien et al. 2002) and 2008 (Moum et al. 2011). An intriguing phenomenon consistently observed in this system is the deep-cycle turbulence that extends beyond the surface mixed layer into the pycnocline where the gradient Richardson number Ri_g is marginally stable. The turbulence occurs in bursts preferentially during nighttime and generates patches of elevated dissipation rate ε. The dissipation rate is up to three orders of magnitude larger inside the patches. Observed deep-cycle turbulence is also reported to be strongly correlated with narrowband near-N oscillations. The oscillations are suggested to be either downward-propagating internal waves excited by dynamics at the base of the surface mixed layer or an intermittent shear instability local to the EUC.

While there have been contrasting theories on how the deep-cycle turbulence occur (McPhaden and Peters 1992; Wijesekera and Dillon 1991), recent studies suggest that shear instabilities are the most probable cause (Lien et al. 2002; Moum et al. 2011; Pham et al. 2012). Recent field observations (Moum et al. 2011) and corresponding linear stability analysis (Smyth et al. 2011) have shown that shear instabilities can occur "deep" in the EUC. These modes of instability were suggested to grow intermittently due to random variations in the EUC background condition that cause Ri_g to fall below the critical value of 0.25. The growth of such instabilities is then assumed to cause isopycnals in the EUC to oscillate at a near-N frequency. While not explicitly demonstrated, the studies imply that the process leading to deep-cycle turbulence is similar to the nonlinear evolution of Kelvin–Helmholtz (K–H) billows

Corresponding author address: Hieu T. Pham, Department of Mechanical and Aerospace Engineering, University of California, San Diego, 9500 Gilman Dr., La Jolla, CA 92092.
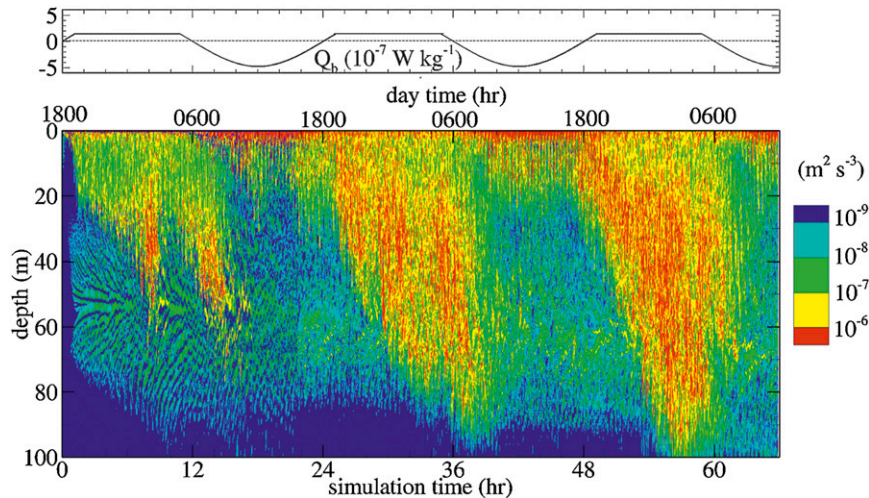E-mail: h8pham@ucsd.edu

FIG. 1. (top) The surface buoyancy flux is plotted. (bottom) Time evolution of the dissipation rate along a vertical pencil shows the diurnal cycle of deep-cycle turbulence in the upper flank of the EUC. Each night, bursts of turbulence are seen between 1800 and 0800 LT of the following morning. The bursts cause patches of elevated dissipation rate extending down to 90-m depth. The elevation of dissipation rate is up to three orders of magnitude compared to the value during daytime at the same depth.

(Smyth et al. 2001). This implication was supported by the large-scale overturn of a wave crest previously observed in Hebert et al. (1992). Alternately, the direct numerical simulation (DNS) of Pham et al. (2012) showed that the near-N oscillations can be caused by the development of a Holmboe shear instability at the base of the surface layer. The breakdown of the Holmboe instability through a secondary shear instability, followed by downward penetration of three-dimensional horseshoe vortices, leads to turbulence at depth. Of interest, and still unanswered, in this scenario is how the background shear and stratification change in order to support the growth of a shear instability. The role of surface wind and buoyancy forcing in establishing the diurnal cycle of turbulence in a region substantially below the surface mixed layer also remains an outstanding question.

Large-eddy simulations (LESs) have been used previously to investigate dynamics of the EUC. For example, Skyllingstad and Denbo (1994) performed an LES with profiles of shear and stratification taken from field measurement, a steady wind stress, and a diurnal heat flux. A simulation of a 3-day period showed that the nighttime oscillations were a signature of shear instabilities in the surface mixed layer. In another simulation at finer resolution, but for only few hours, the oscillations were shown to break at the base of the surface mixed layer at 20–30-m depth via a K–H shear instability process. The occurrence of deep-cycle turbulence at greater depths and its diurnal cycle was not simulated in this study. In another LES study, Wang et al. (1998) modeled a similar EUC system with several additional

forcing components. A simulation of 6 days showed a diurnal cycle of turbulence at depth as large as 60 m. The study suggested that the deep-cycle turbulence resulted from shear instabilities; however, the dynamical processes involved were not identified. The generation of the near-N oscillations were absent because the horizontal domain was too short to resolve this scale. In a later study, Wang and Muller (2002) extended the domain, but the model was simplified with only shear and stratification profiles and a steady (not diurnal) surface buoyancy flux. In this study, nighttime convective plumes were shown to penetrate deep into the EUC and to cause a shear instability. Isopycnal oscillations and an increase in fluctuation kinetic energy were shown; however, the evolution of turbulence was not described.

It is evident that observational data and LES results to date have not provided a complete description of the life cycle of deep-cycle turbulence. At the same time, DNS studies focusing on the mixing processes lack the large-scale environmental forcing. It is of interest to have an LES study in which both the large-scale forcing and the small-scale turbulent processes are allowed to interact, and that is the goal of the present investigation. Here, we use results from a high-resolution LES model of the EUC to investigate the dynamical processes leading to deep-cycle turbulence. The model is initiated with shear and stratification profiles similar to what is observed in the EUC. A steady westward wind stress and a diurnal buoyancy flux are applied at the surface. Results from the model indicate the generation of both near-N oscillations and deep-cycle turbulence. Figure 1 shows the

time evolution of the computed dissipation rate taken along a vertical pencil, similar to a mooring. The high-resolution LES has enabled numerical simulation, for the first time, of the diurnal cycle of deep-cycle turbulence showing consistent bursts of deep-cycle turbulence with elevated dissipation rate at depths well below the surface layer between 1800 and 0600 LT.

The remainder of the paper is arranged as follows. The model formulation and the numerical method are provided in section 2. The diurnal variation in the dissipation rate is described in section 3. The variability in the mean shear and stratification in response to the surface forcing is discussed in section 4 to explain why the turbulence bursts preferentially occur at nighttime. The bursts of deep-cycle turbulence in Fig. 1 are preceded by near-N oscillations, which are discussed in section 5. In section 6, we track the evolution of the shear instabilities from their growth to their collapse leading to the deep-cycle turbulence. We conclude by pointing out key differences between our results and previous studies in section 7.

2. Model formulation

a. Flow condition

The present study focuses on the interaction between surface forcing and a background flow similar to observational data. The surface forcing consists of a steady (in time and in space) westward wind stress $\tau_w = 0.1\,\mathrm{N\,m^{-2}}$ and a diurnal surface buoyancy flux. The zonal velocity u is composed of a westward flowing South Equatorial Current (SEC) and an eastward-flowing EUC jet with a peak velocity of $0.9\,\mathrm{m\,s^{-1}}$ at 110-m depth. The meridional flow is excluded in our model. The density ρ is initialized with a surface mixed layer of approximately 25-m depth and a pycnocline between depths of 25 and 150 m. The deeper ocean is weakly stratified. The explicit expressions for shear rate $S = d\langle u\rangle/dz$ and squared buoyancy frequency $N^2 = -g/\rho_0 d\langle\rho\rangle/dz$ are given as follows:

$$S(z) = 0.9\tanh\left(\frac{z+25.0}{10.0}\right) - 1.35\tanh\left(\frac{z+110.0}{15.0}\right)$$
$$+ 0.45\tanh\left(\frac{z+225.0}{25.0}\right), \quad (10^{-2}\,\mathrm{s^{-1}}), \quad \text{and} \tag{1}$$

$$N^2(z) = -0.5\tanh\left(\frac{z+25.0}{10.0}\right) + 0.3\tanh\left(\frac{z+150.0}{25.0}\right)$$
$$+ 0.2, \quad (10^{-4}\,\mathrm{s^{-2}}). \tag{2}$$

Here, g is gravity, and the angle brackets $\langle\cdot\rangle$ denote averaging in the zonal x and the meridional y directions.

During daytime, the surface buoyancy flux varies sinusoidally with a peak negative value of $Q_b = 4.8 \times 10^{-7}\,\mathrm{W\,kg^{-1}}$ at noon. The buoyancy flux is neutral at 0600 and 1800 LT and has a constant value of $Q_b = 1.245 \times 10^{-7}\,\mathrm{W\,kg^{-1}}$ from the early evening at 1900 LT until the early morning of the next day at 0500 LT. The buoyancy flux corresponds to a heating flux of $796\,\mathrm{W\,m^{-2}}$ at noon and a cooling flux of $206\,\mathrm{W\,m^{-2}}$ during nighttime. The selection of the surface forcing, as shown in the top panel of Fig. 1, and the EUC flow condition, shown in Fig. 2, is consistent with the observational data of the EUC reported in Moum et al. (2011) as well as the values used in the LES model of Wang and Muller (2002). It is noted that observational data indicates substantial spatial and temporal variabilities in the shear and stratification profiles of the EUC, and therefore, our model only presents one such initial condition. The model is driven for a 3-day period during which the zonal velocity and the density vary considerably from their initial conditions, and we find the presence of deep-cycle turbulence in all three nights.

b. Mathematical model

The governing equations for the zonal velocity (i.e., u), meridional velocity v, vertical velocity w, and density (i.e., ρ) are the three-dimensional Boussinesq equations for stratified flows with an LES subgrid model, and they take the following form:

$$\frac{\partial u_i}{\partial x_i} = 0, \tag{3}$$

$$\frac{\partial u_i}{\partial t} + \frac{\partial}{\partial x_j}(u_i u_j) = -\frac{1}{\rho_0}\frac{\partial P}{\partial x_i} - \frac{g\rho\delta_{i,3}}{\rho_0} + \nu\frac{\partial^2 u_i}{\partial x_j \partial x_j}$$
$$-\frac{\partial\tau_{ij}}{\partial x_j} + \frac{\partial}{\partial x_j}\left(\frac{\tau_w}{\rho_0}\right), \quad \text{and} \tag{4}$$

$$\frac{\partial\rho}{\partial t} + \frac{\partial}{\partial x_j}(\rho u_j) = \frac{\partial}{\partial x_j}\left[(\kappa + \kappa_{\mathrm{sgs}})\frac{\partial\rho}{\partial x_j} + \frac{\rho_0 Q_b}{g}\right]. \tag{5}$$

Here, ν and κ are molecular viscosity and thermal diffusivity of water, respectively, and S_{ij} is velocity strain rate. An LES procedure with a Smagorinsky subgrid parameterization scheme is used to obtain the subgrid stress τ_{ij} as follows:

$$\tau_{ij} = -2\nu_{\mathrm{sgs}}S_{ij} = -2C_{\mathrm{sgs}}^2\Delta^2|S_{ij}|S_{ij}, \tag{6}$$

where ν_{sgs} is subgrid viscosity and the model coefficient C_{sgs} is set to be 0.15. The modulus of the strain rate $|S_{ij}| = \sqrt{2S_{ij}'S_{ij}'}$ is computed using only fluctuating
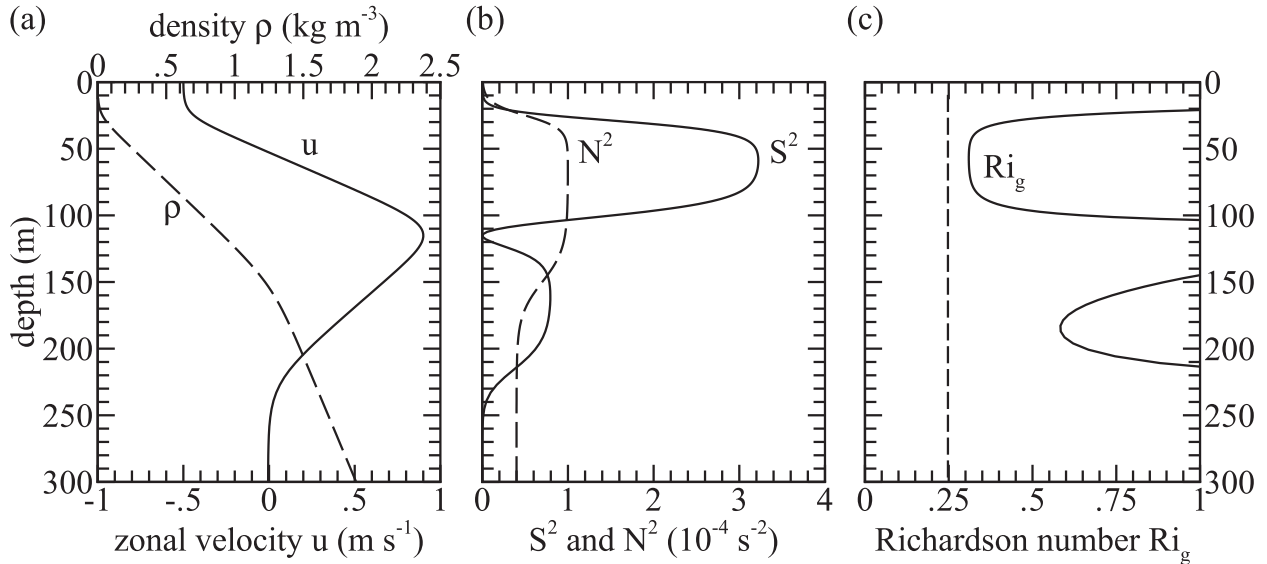
FIG. 2. Initial mean profiles. (a) The velocity consists of a surface current (SEC) moving westward in an opposite direction to an undercurrent (EUC) with a peak velocity $U_j = 0.9\,\mathrm{m\,s}^{-1}$ at 110-m depth. (b) The stratification profile N^2 corresponds to a surface layer, an upper thermocline, and a lower thermocline. (c) The gradient Richardson number Ri_g is larger than 0.25 at all depths. A steady wind stress and a diurnal buoyancy flux are applied at the surface.

velocities. The filter width Δ is taken to be $\sqrt{\Delta x_i^2}$, where Δx_i is the grid spacing. The subgrid diffusivity κ_{sgs} is set such that the subgrid Prandtl number $\mathrm{Pr}_{\mathrm{sgs}}$ is equal to 1.

The governing equations are integrated using a second-order finite difference in space and third-order Runge–Kutta marching in time. The computational domain has 960 m in the zonal x direction, 80 m in the meridional y direction, and 415 m in the vertical z direction. The domain is discretized at $\Delta x = \Delta y = 1.25$-m resolution in the horizontal directions. A vertical grid of 384 points has a uniform spacing of $\Delta z = 25$ cm in the region shallower than 64 m, followed by a grid stretching of 3% below this depth. The zonal length of our domain is comparable to that of Wang and Muller (2002), and our resolution is sufficiently finer, so that our model is able to resolve both the long scale of the oscillations as well as the small overturning scales during the evolution of shear instabilities. The model assumes periodicity in the horizontal directions and a sponge layer is employed between depths of 265 and 415 m to prevent wave reflection from the bottom boundary.

c. Boundary conditions

To enforce horizontal periodicity, all flow variables f satisfy

$$f(x, y, z) = f(x + L_x, y, z) = f(x, y + L_y, z), \qquad (7)$$

where L_x and L_y are the lengths of the simulated domain in the zonal and meridional directions, respectively. At the surface, the steady wind stress and diurnal buoyancy flux are enforced. The horizontal velocities (i.e., u and v) and density (i.e., ρ) are set as follows:

$$\left.\frac{\partial u}{\partial z}\right|_{z=0} = \left.\frac{\partial v}{\partial z}\right|_{z=0} = \left.\frac{\partial \rho}{\partial z}\right|_{z=0} = 0. \qquad (8)$$

The no-penetration condition is enforced at the surface by setting

$$w|_{z=0} = 0. \qquad (9)$$

At the lower boundary, similar conditions are used on the velocities while the density has a constant gradient such that $N^2 = 4.0 \times 10^{-5}\,\mathrm{s}^{-2}$.

d. Statistical analysis

Different from observational analysis in which statistics are obtained through temporal averaging, our model assumes horizontal periodicity so that statistics are computed using spatial averages over the horizontal x–y plane. The model outputs three-dimensional fields of velocity, pressure, and density instantaneously. These fields are decomposed into a mean quantity, denoted by angle brackets $\langle\cdot\rangle$, and a fluctuation quantity, denoted by a prime. The latter includes contributions from both oscillations (waves) and turbulence. In the following sections, we use the mean quantity to discuss the temporal variation in the background flow conditions while the fluctuation quantity is used to analyze turbulence statistics.

3. Temporal variability of turbulent dissipation rate

Three sources of turbulence are seen in the model: wind-, convection-, and shear-driven, and the evolution of turbulence in the surface layer is considerably different from that in the EUC. In this section, the temporal evolution of the dissipation rate, defined as $\varepsilon = 2\nu S'_{ij} S'_{ij} - \tau'_{ij} S'_{ij}$, is used to differentiate among different sources of turbulence. At 10-m depth, the dissipation rate shown in Fig. 1 has the following daily trend, especially during the last two nights: low values having magnitude on the order of $10^{-8}\,\mathrm{m^2\,s^{-3}}$ during daytime between 1000 and 1600 LT, a two-order-of-magnitude increase to $10^{-6}\,\mathrm{m^2\,s^{-3}}$ in the evening between 1600 and 0000 LT, and an intermediate value of $10^{-7}\,\mathrm{m^2\,s^{-3}}$ between 0000 and 1000 LT of the following day. In the late morning and the afternoon, the negative surface buoyancy flux stabilizes the surface layer and the turbulence generated by the wind stress is reduced. In the late afternoon, at approximately 1600 LT, when the surface buoyancy flux relaxes toward neutral level, the shear generated by the wind in the surface layer becomes unstable and causes a rapid increase in the dissipation rate. After midnight, convection drives turbulence in the surface layer, and the resulting dissipation rate is approximately an order of magnitude smaller than that of the late afternoon wind-driven turbulence.

The dissipation rate in the EUC shows bursts of deep-cycle turbulence during nighttime, similar to what is found in observations. Patches of elevated dissipation rate occur at depths in the EUC as shown in Fig. 1. The patches during the first night are relatively small and weak, while those during the following two nights are more consistent in terms of turbulent intensity, vertical extent, and temporal duration. The dissipation rate inside the patches is on the order of $10^{-6}\,\mathrm{m^2\,s^{-3}}$, which is comparable to value obtained in the observations of Moum et al. (1992), Lien et al. (2002), and Moum et al. (2011). The patches extend down to 90-m depth. These patches of turbulence are driven by shear instabilities whose evolution is to be described in section 6. During the evening of each day as the wind-driven shear in the surface layer becomes unstable, the lower boundary of the region of elevated dissipation rate descends from the surface layer down into the core of the EUC. Between midnight and the morning, the dissipation rate in the EUC is larger than that in the surface layer where convective turbulence dominates. The turbulence in the EUC subsides during the morning when the surface buoyancy flux stabilizes the surface layer. The dissipation rate of shear-driven turbulence at depth in the EUC is comparable to that of the wind-driven turbulence but considerably larger than that of convective turbulence.

4. Temporal variability of mean shear and stratification

Previous studies suggest that deep-cycle turbulence results from intermittent shear instabilities (Lien et al. 1996; Moum et al. 2011). Occasionally, variations in shear and stratification cause the gradient Richardson number to fall below the critical value of 0.25 and a shear instability develops. The cause for such a reduction remains ambiguous, that is, whether due to an enhancement in shear rate or due to a reduction in the stratification. Furthermore, the relation of the reduced Richardson number to external forcing remains unclear. In this section, we will show that a region of enhanced shear with an Ri_g below 0.2 moves downward when the surface forcing changes from heating to cooling. This sheared region interacts with the marginally stable EUC shear to enable deep-cycle turbulence in the night.

Time evolution of the squared buoyancy frequency (i.e., N^2) along a vertical pencil at $x = 480\,\mathrm{m}$ and $y = 40\,\mathrm{m}$ is shown in Fig. 3b. The N^2 has a low value in the surface layer during nighttime and a larger value during daytime when the negative surface buoyancy flux stratifies the layer. Between the hours of 1800 and 2000 LT of each evening, the stratification at the 20-m depth rapidly decreases. Although the surface buoyancy flux begins to have a negative value at this time, the mixing is not convection driven but rather shear driven. The white solid lines in Fig. 3b indicate isocontours of neutral N^2. At any instant, the region lying above this line has a positive density gradient, caused by positive surface buoyancy flux. In our simulation, the convectively unstable layer reaches a maximum depth of approximately 10 m, which is considerably shallower than the 25 m surface mixed layer of Wang and Muller (2002). In that study, convective plumes penetrate down to 30-m depth and generate turbulent kinetic energy at this depth. In the present study, the shear instabilities leading to deep-cycle turbulence are not triggered by a reduction in stratification due to convective mixing but by an increase in the shear rate at the base of the mixed layer in the late afternoon.

Distinct differences in values of the squared mean shear rate S^2 between day- and nighttime in the surface layer are shown in Fig. 3c. Although the wind stress in our model is steady in time, momentum input into shear is different between day- and nighttime because the momentum mixing rates are different. Over a 24-h period, S^2 is relatively small in the top 20 m surface layer during nighttime between 1800 and 0600 LT when the convective turbulence actively mixes the momentum. The S^2 increases in this layer during daytime, as a result of the steady wind stress and a lack of convective mixing.
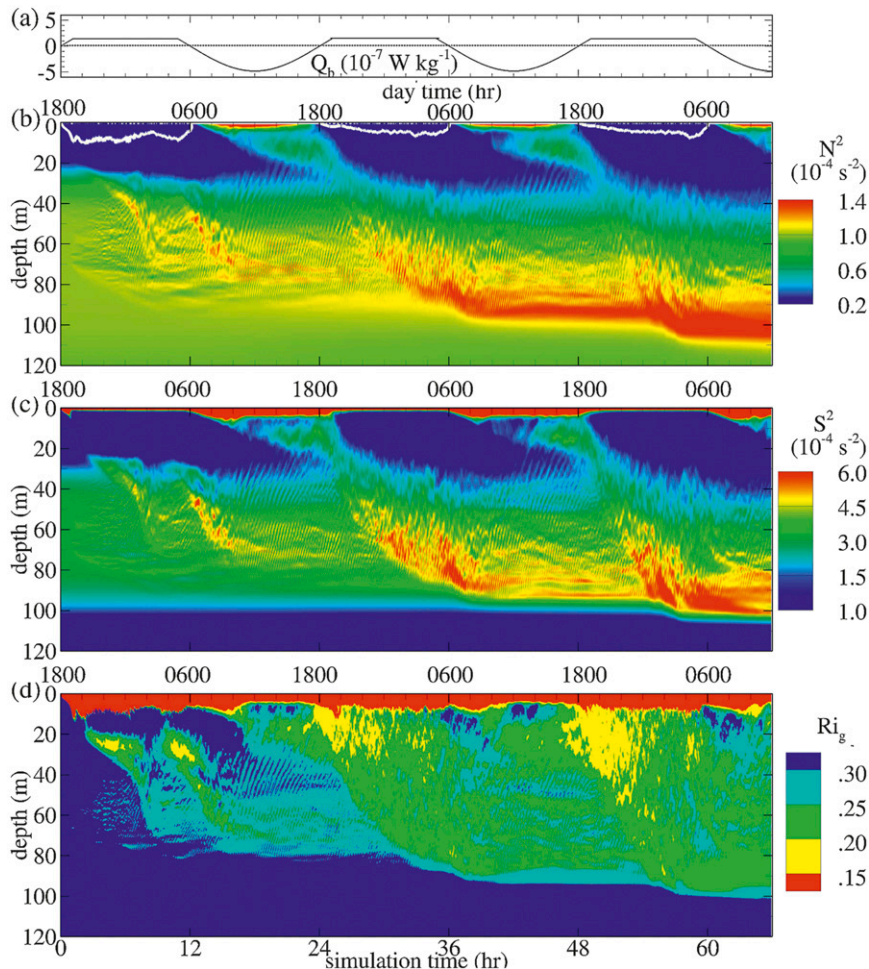
FIG. 3. Evolution of (a) surface buoyancy flux, (b) N^2, (c) S^2, and (d) Ri_g along a vertical line at a fixed horizontal location, $x = 480$ and $y = 40$ m. The evolution between nights two and three is qualitatively similar. A region of stratified shear with an Ri_g less than 0.2 is seen to move downward during the evening when the surface heating relaxes. White solid lines in (b) indicate depths above which N^2 is negative.

Other turbulence-generation processes absent in our model such as surface wave breaking can cause a higher mixing rate during daytime, and the shear rate would be weaker in such cases. In the present study, the negative surface buoyancy flux during daytime stabilizes the surface layer, and the wind stress accelerates the SEC resulting in an increase in the shear rate.

Daily, the surface region with high shear rate has deepened to 25-m depth by approximately 2000 LT as shown in Fig. 3c. At this time, the shear rate rapidly decreases in the surface layer, while the shear below commences to increase. The stratified sheared region originates from the base of the surface layer approximately at 25-m depth and descends downward into the core of the EUC. The burst in shear at each depth is correlated to the patches of elevated dissipation rate

discussed in the preceding section. Observational data from Moum et al. (2011) and Smyth et al. (2013) also indicate bursts in the squared shear rate deep in the EUC; however, the bursts in our model have a larger vertical extent. In section 6, we will show that these nightly bursts in the shear rate generate shear instabilities leading to deep-cycle turbulence. The wind inputs momentum into the mean shear in the surface layer throughout the morning and the afternoon. The shear in turn becomes unstable and mixes both the momentum and the density in the layer in the late afternoon. The mechanism of mixing is through shear instabilities; however, the shear is built up from the wind stress. We refer to the resulting turbulence as wind driven in the last section. In contrast, the deep-cycle turbulence that occurs in our model is driven by shear in the mean

currents at a much greater depth. Over the three-night period, Figures 3b and 3c show a secular trend of decreasing N^2 and S^2 in the region between depths of 25 and 100 m. This is due to the mixing of deep-cycle turbulence in absence of large-scale forcing such as upwelling and horizontal pressure gradient to keep the zonal flow in balance.

The trigger for the initiation of deep-cycle turbulence is the evening burst of shear (commences at about 1800 LT as discussed in the previous paragraph) that creates a stratified layer with $Ri_g < 0.2$ at the base of the mixed layer. We now discuss the evolution of Ri_g shown in Fig. 3d. The variations in shear and stratification cause Ri_g during the last two nights to be different from the initial values. Initially, Ri_g has a value greater than 0.3 at all depths. Because of mixing during the first night, Ri_g decreases to smaller values, clustering generally in the range of 0.2–0.3 in the region between depths of 20 and 90 m. When the dissipation rate is elevated in the EUC, Ri_g has values in the range of 0.2–0.25. However, there are many instances when $0.2 < Ri_g < 0.25$ in the EUC and turbulence does not develop. Similarly, during the afternoons, beginning from noon to 1800 LT, Ri_g at 20-m depth has a value less than 0.25 but larger than 0.2, and shear instabilities do not grow. When Ri_g dips below 0.2 in the late afternoon, shear instabilities develop at this depth causing elevated dissipation rate as was shown in Fig. 1. Therefore, $Ri_g < 0.2$ is found to be indicative of the growth of shear instabilities leading to deep-cycle turbulence in our model. This does not contradict linear stability theory, which states that a flow is stable when $Ri_g(z)$ is greater than ¼ at all depths. Furthermore, linear stability theory assumes steady profiles of shear and stratification while the flow is unsteady on a time scale comparable to that of the turbulence evolution in the present study. It is also worth noting that values of critical Richardson number less than 0.25 have been found in the context of other flows, for example, uniform shear flow (Jacobitz et al. 1997).

The diurnal cycle of N^2, S^2, and Ri_g in the surface layer in the present model agrees with the observational data collected during Tropic Heat I and Tropic Heat 2 experiments. Peters et al. (1994) found a diurnal cycle in the upper-equatorial ocean including in the turbulent dissipation rate, finescale shear variance, buoyancy frequency, and gradient Richardson number. The observed cycle extends beyond the surface mixed layer into the pycnocline. The authors suggested that the nighttime enhancement in the finescale shear in the surface layer is the key element in controlling mixing in the pycnocline. However, it is unclear whether the finescale shear is associated with the near-N internal waves or shear instability. Results from our model indicate that the diurnal

variations in the surface layer control shear instabilities that lead to bursts of deep-cycle turbulence in the EUC. The burst occurs in the late afternoon when the shear at the base of the surface layer increases and triggers a thickening region of enhanced shear, reduced Ri_g, and concomitant turbulence. It is of interest to understand why the shear rate increases, and we will return to this point in section 6.

5. Near-N oscillations

It has been established that deep-cycle turbulence is correlated with near-N oscillations in the isopycnals (Moum et al. 1992; Lien et al. 2002). Smyth et al. (2011) suggested that the oscillations are a signature of shear instabilities with critical levels deep in the EUC regions. In Pham et al. (2012), we showed that a shear instability at the base of the surface mixed layer can have the tail of its eigenfunction extend into the EUC and cause near-N oscillations at depth. In the present simulation, the bursts of deep-cycle turbulence are also preceded by the appearance of near-N oscillations. In this section, we focus on the oscillation and turbulence events during the third night to illustrate the characteristics of such oscillations. The oscillations are also present during the second night and show similar characteristics.

The density records at five different depths in the EUC, shown in Fig. 4, illustrate the origin and subsequent evolution of deep-cycle turbulence during the third night. The high-frequency fluctuations indicating turbulence appear first in the 40-m record and migrate downward to greater depths in time. Similar to previous observational studies (Moum et al. 1992; Lien et al. 2002; Moum et al. 2011), the burst of turbulence in our model is preceded by the presence of isopycnal oscillations. Between the hours of 1700 and 2300 LT, a few cycles of the oscillations are seen in the records between depths of 60 and 80 m. Despite the variation of zonal velocity, including opposite signs between depths of 50 and 80 m, the oscillations propagate westward at all depths. The oscillations are vertically coherent across the three density records with the troughs and crests occurring at the same time in the three records. The observation of Hebert et al. (1992) presented a wave packet of which the middle wave crest overturns resulting in turbulence. In the present study, the density records in Fig. 4 also exhibits multiple wave crests and troughs; nevertheless, their amplitude is significantly smaller and none of them overturns. The higher-frequency turbulent fluctuations seen in the records at depths after midnight result from development of secondary shear instabilities with similarities to that discussed in Pham et al. (2012).
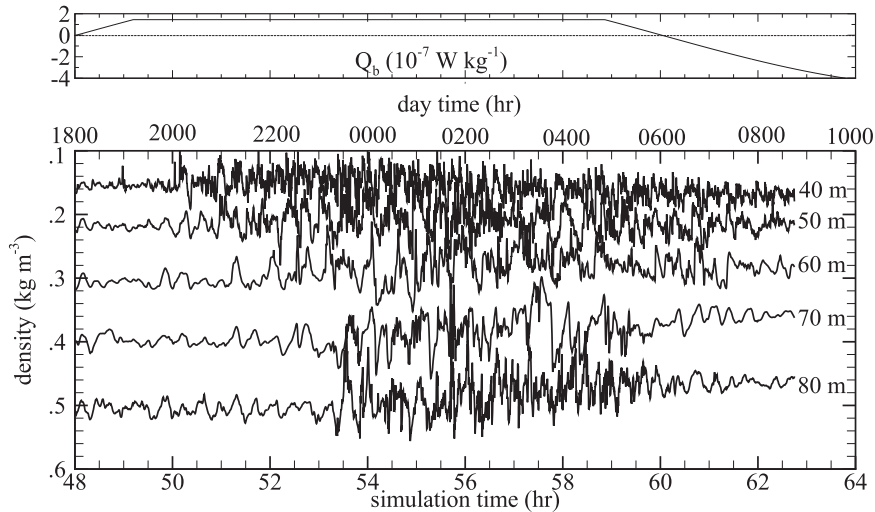
FIG. 4. (top) The surface buoyancy flux is plotted. (bottom) Evolution of the density at $x = 480$, $y = 40\,m$ and five different depths during the third night. Broadband high-frequency turbulent fluctuations originate from the base of the surface mixed layer and descend downward. The fluctuations are preceded by vertically coherent narrowband near-N oscillations.

The x–t diagrams in Fig. 5a indicate that the oscillations have a westward phase velocity. In the diagrams, the density record along the zonal direction at 80-m depth is plotted versus time. At 80-m depth, the zonal flow is eastward; however, the oscillations have phase lines tilted westward (leftward in the plot). The power spectrum of the density record, shown in Fig. 5b, has a narrowband frequency of $\omega = 0.004$–$0.005\,Hz$ and a narrowband wavenumber of $k_x = 0.0065$–$0.02\,m^{-1}$. The frequency of the oscillations is slightly smaller than the background buoyancy frequency in the EUC. The corresponding wavelength of the oscillations has a range of 314–960 m. The range of wavelengths in our model is larger than the values reported in observational data. Moum et al. (1992) estimated a wavelength in the range of 150– 250 m, and the wave packet in Hebert et al. (1992) had an estimated wavelength of 100 m. The estimate was 360 m in Lien et al. (2002). Moum et al. (2011) found a median value for the most unstable wavelength to be 248 m and a maximum value of 340 m by performing
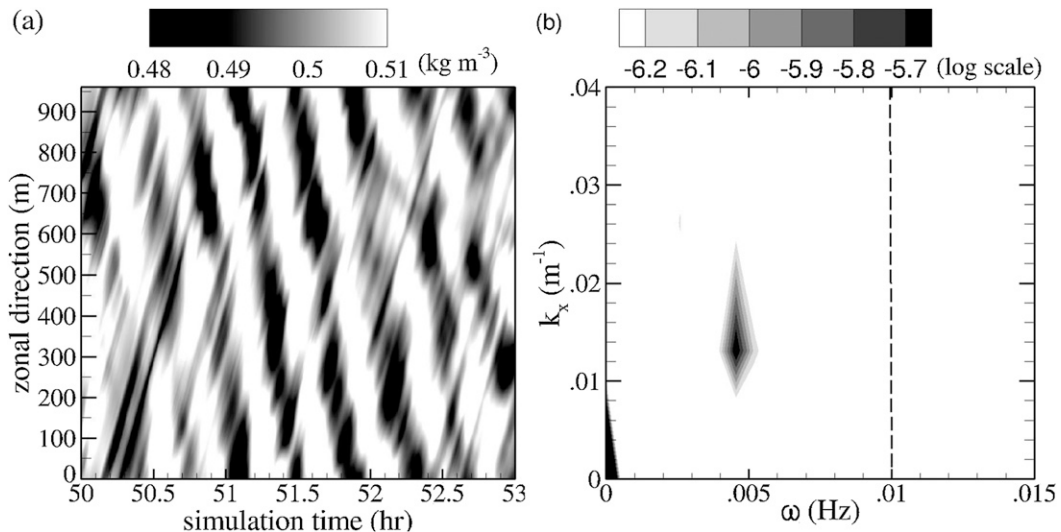

FIG. 5. (a) Time evolution of the density along the zonal direction at $y = 40$ and $z = 80\,m$ during the early evening of the third night shows westward-propagating phase lines; (b) power spectrum shows a narrow frequency band in range of $\omega = 0.004$–$0.005\,Hz$ and a narrow horizontal wavenumber range $k_x = 0.01$–$0.02\,m^{-1}$. The dashed line in (b) denotes the background buoyancy frequency value N at the same depth.
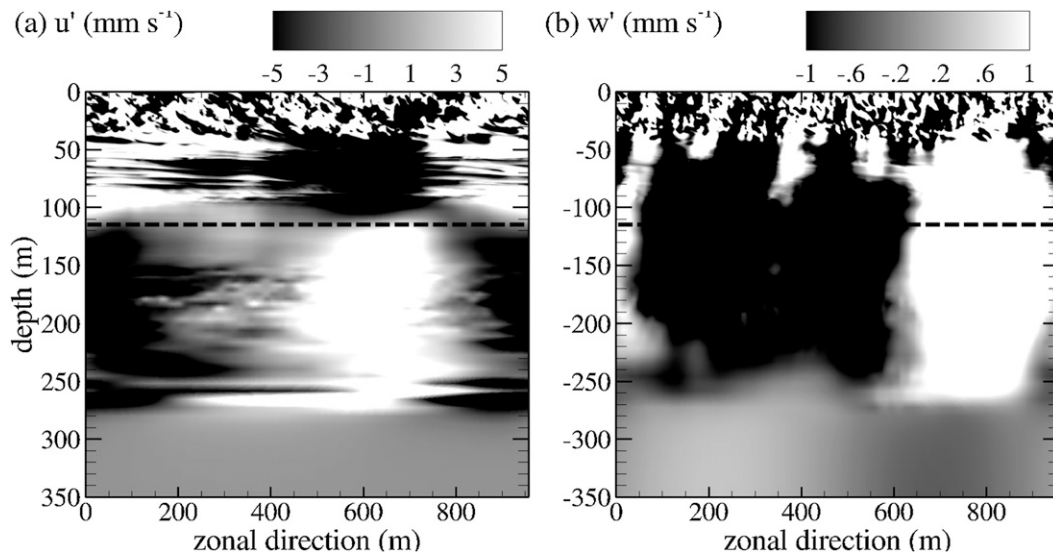
FIG. 6. Spatial structure of the near-N oscillations in the EUC: (a) u' and (b) w' at 2000 LT during the third night. The horizontal dashed lines denote the depth at which the peak eastward zonal velocity occurs. At this depth, the amplitude of w' has a local max while the amplitude of u' attenuates. The oscillations are trapped in the lower flank of the EUC and do not extend to greater depth.

linear stability analysis on an ensemble of observed shear and stratification profiles.

Linear stability theory indicates that the unstable shear mode has its phase speed equal to the zonal velocity at the depth at which the instability grows. In our model, the oscillations have a westward phase speed, $c = \omega/k$, with a range of 0.2–0.77 m s^{-1} suggesting that the shear instability, which causes the oscillations, has originated at the base of the surface layer. The characteristics of the near-N oscillations and the mean profiles of zonal velocity and stratification at the time when the oscillations develop in the present model are similar to what we had seen in Pham et al. (2012) and the signal of a Holmboe wave at depth is clear in both studies. But there is a difference in the shear instabilities that occur in the subsurface stratified shear layer. In that study, because the simulation was performed at a low Reynolds number and the Holmboe shear instability was allowed to grow from a quiescent background in absence of the surface forcing, the structure of the Holmboe shear instability was clearly identified. In the present LES simulation at a high Reynolds number, the turbulence caused by the surface forcing in the surface layer is so strong that the cusps of the nonlinearly evolving Holmboe waves are not present and, furthermore, the shear and stratification profiles are more complex. The initial instabilities in the subsurface region are likely of multiple families and not dominated by either K–H or Holmboe instabilities. In this point, we refer the readers to previous works on Holmboe instability (Holmboe 1962; Smyth and Peltier 1989) and

specifically the study of Carpenter et al. (2007) who showed the transition from K–H to asymmetric Holmboe instability when the background profiles are slightly altered.

The oscillations originate at the base of the surface layer and extend into the lower flank of the EUC as shown in Fig. 6. In the figure, both the fluctuating zonal velocity u' and fluctuating vertical velocity w' fields show vertical phase lines extending from 40- to 270-m depth. The vertical phase lines propagate westward in the opposite direction of the local eastward velocity. At the 115-m depth, where the peak eastward zonal velocity occurs, the amplitude of u' attenuates while the amplitude of w' locally peaks. Pham et al. (2012) have discussed a similar behavior of linear internal waves propagating in a background with continuously varying shear and stratification. It is noted that the properties of the oscillations seen in our model are constrained by the horizontal extent of our domain. Our model only allows shear instabilities having a wavelength shorter than 960 m to grow. It is possible that the oscillations can have a larger wavelength and extend deeper beyond the EUC when a larger domain is used.

6. Evolution of shear instabilities

We have discussed in section 4 that the temporal variability in the mean shear rate and the stratification favors shear instability as the triggering process for the deep-cycle turbulence. Previous studies, which suggest shear instability as a cause of the near-N oscillations,
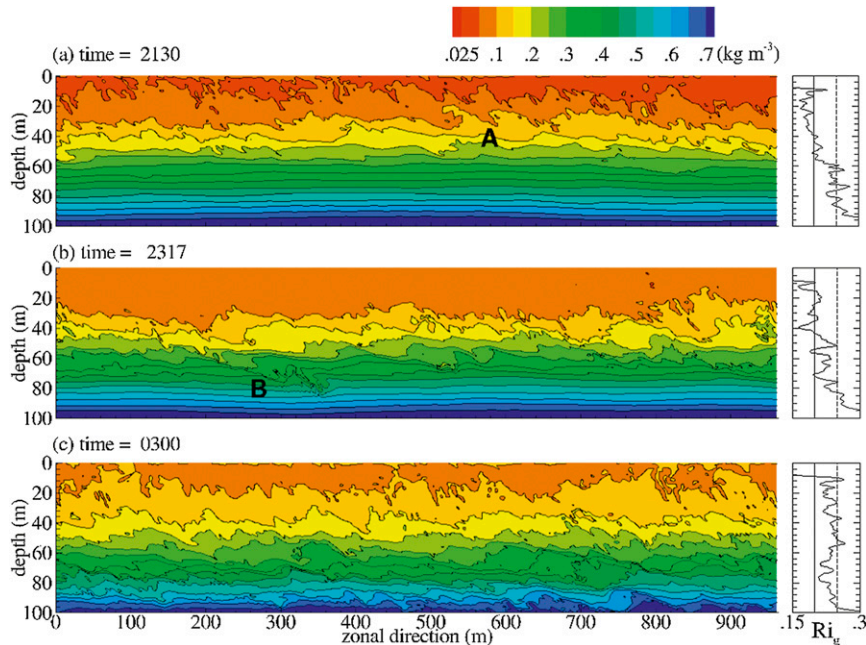
FIG. 7. Snapshots of the density field at three different times showing the generation and deepening of deep-cycle turbulence during the third night: (a) isopycnal overturns denoted by letter "A" resemble K–H billows; (b) a vortex denoted by letter "B" originates at 60-m depth and penetrates downward to 80-m depth; and (c) the downward vortex penetration causes the entire upper flank of the EUC to become turbulent. (right) Vertical profiles of the Ri_g are shown, and dotted and dashed lines indicate values of 0.25 and 0.2, respectively.

often take the instability to be a random event (Lien et al. 2002; Moum et al. 2011). An explanation of how the flow becomes favorable for instability is lacking. Furthermore, many studies suggest the breakdown of oscillation-scale K–H shear instability as the evolutionary process leading to deep-cycle turbulence. Alternately, Pham et al. (2012) demonstrated that the process can involve a complex cascade of shear instabilities. In this section, the evolution of the instability events, which begins with the narrowband near-N oscillations resembling a Holmboe wave, is presented.

Snapshots of the density field at three different times depicting the evolution of the deep-cycle turbulence during the third night are shown in Fig. 7. The corresponding profiles of gradient Richardson number are shown in the right panels. Soon after the appearance of the near-N oscillations, which occur during the early evening as discussed in the last section, shear instability develops at the base of the surface layer. Denoted by letter "A" in Fig. 7a, two K–H-like overturns occur next to each other at 30-m depth where the mean value of $Ri_g < 0.2$. The horizontal wavelength, on the order of 100 m, of the shear instability is shorter than the wavelength of the near-N oscillations and the vertical extent of the overturns is approximately 20 m. The wavelength

of the secondary shear instability in our model is in the same range with the most unstable shear modes in the linear stability analysis of Smyth et al. (2011) using the observed profiles of velocity and stratification.

The descent of the deep-cycle turbulence into the core of the EUC is associated with vortices that form at the bottom of the K–H-like overturns as shown in Fig. 7b. In the figure, a vortex that was translating westward at 50-m depth is stretched downward and eastward by the preexisting EUC shear causing a localized patch of turbulence denoted by letter "B." The formation of billows and the downward penetration of stretched vortical structures generate turbulence and cause enhanced dissipation rate as deep as 90 m. Downward vortex penetration in a similar manner that has been reported in the studies of Pham and Sarkar (2010) and Pham et al. (2012). The penetration further tips the stability condition in the EUC where Ri_g is marginally stable at an earlier time. Figure 7c shows mixing in the entire upper flank of the EUC down to 100-m depth. As the turbulence subsides, the flow relaxes to a marginally stable state with Ri_g fluctuating in the range of 0.2–0.25. The deep-cycle turbulence in the present study does not result from the direct overturn of the near-N oscillations as was found in Hebert et al. (1992). The turbulence
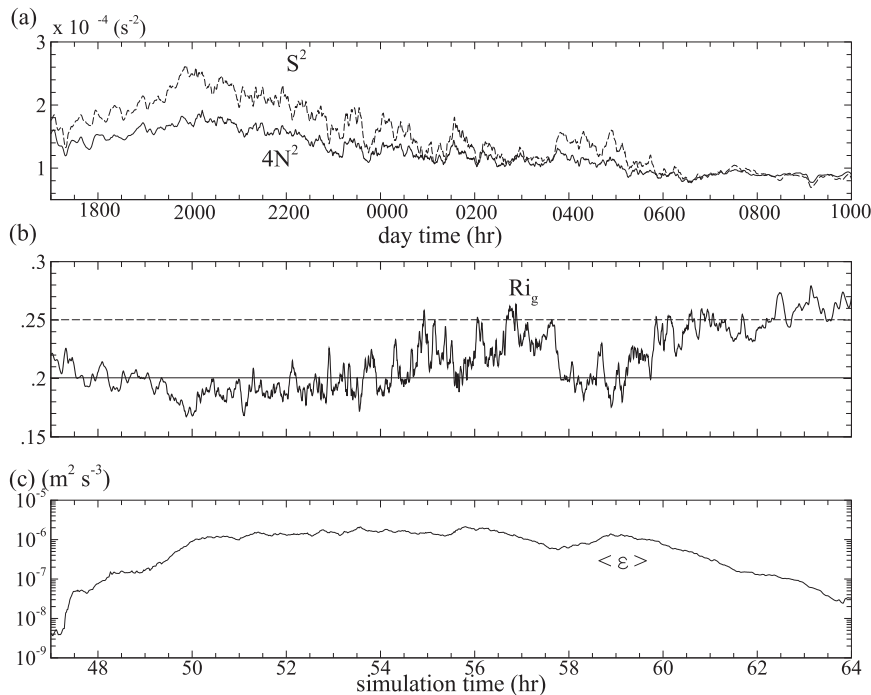
FIG. 8. Temporal variation at 30-m depth during the third night: (a) S^2 and N^2, (b) Ri_g, and (c) horizontally averaged dissipation rate. During the early evening, between 1700 and 2000 LT, S^2 increases while N^2 remains relatively unchanged. As a result, Ri_g decreases to values less than 0.2 leading to shear instabilities and turbulence.

originates from the base of the surface layer with shear instabilities triggered by a decrease in the local gradient Richardson number. We plot the values of N^2 and S^2 at 30-m depth in Fig. 8a and that of Ri_g in Fig. 8b. During the early evening between 1700 and 2000 LT, S^2 increases while N^2 remains mostly unchanged. This causes Ri_g to decrease to a value less than 0.2 and the shear instabilities to grow. During the time period of $Ri_g < 0.2$, the turbulent dissipation rate also increases as shown in Fig. 8c. After 0700 LT in the morning, Ri_g hovers around 0.25 and the turbulent dissipation rate in this marginal state of stratified shear decreases by an order of magnitude.

Such an increase in S^2 can be understood by looking at the relationship between mean zonal flow and turbulent Reynolds stress. The relationship can be described by taking the horizontal average of Eq. (4) and neglecting the surface forcing term. This yields

$$\frac{\partial \langle u \rangle}{\partial t} = -\frac{\partial \langle u'w' \rangle}{\partial z} + \frac{\partial}{\partial z}\left\langle (\nu + \nu_{sgs})\frac{\partial u}{\partial z}\right\rangle. \qquad (10)$$

In this equation, $\langle u'w' \rangle$ is the Reynolds turbulent stress which can alter the background zonal velocity $\langle u \rangle$. The viscous and subgrid stresses on the right-hand side of this equation are at least an order of magnitude smaller than

the Reynolds stress in the present study, so these terms are excluded in the following discussion. Figures 9a–c show the profiles of the mean zonal velocity, the Reynolds stress, and the Reynolds stress vertical divergence, respectively. The profiles are plotted at 1800 and 2000 LT during the third night just right before the deep-cycle turbulence start to descend into the EUC. At 1800 LT, the Reynolds stress has a peak at 10-m depth because of the generation of wind-driven turbulence in the surface layer. The surface buoyancy flux is neutral at this time. As the wind-driven turbulence evolves, the Reynolds stress becomes significantly larger at 2000 LT with the peak deepening to 15-m depth. The divergence of the Reynolds stress is positive in the EUC region between depths of 15 and 60 m at this time. According to Eq. (10), a positive divergence causes the left-hand side of this equation to have negative acceleration. The $\langle u \rangle$ at 2000 LT becomes more negative in this region when compared to the profile at 1800 LT. The westward acceleration increases the shear rate at the base of the surface layer, and thus, drives the shear instabilities shown in Fig. 7. In the present model, the turbulent flux in the surface layer tips the stability condition in the deeper EUC, and thus triggers a rapidly thickening region of stratified shear with reduced Ri_g which leads to the deep-cycle turbulence.
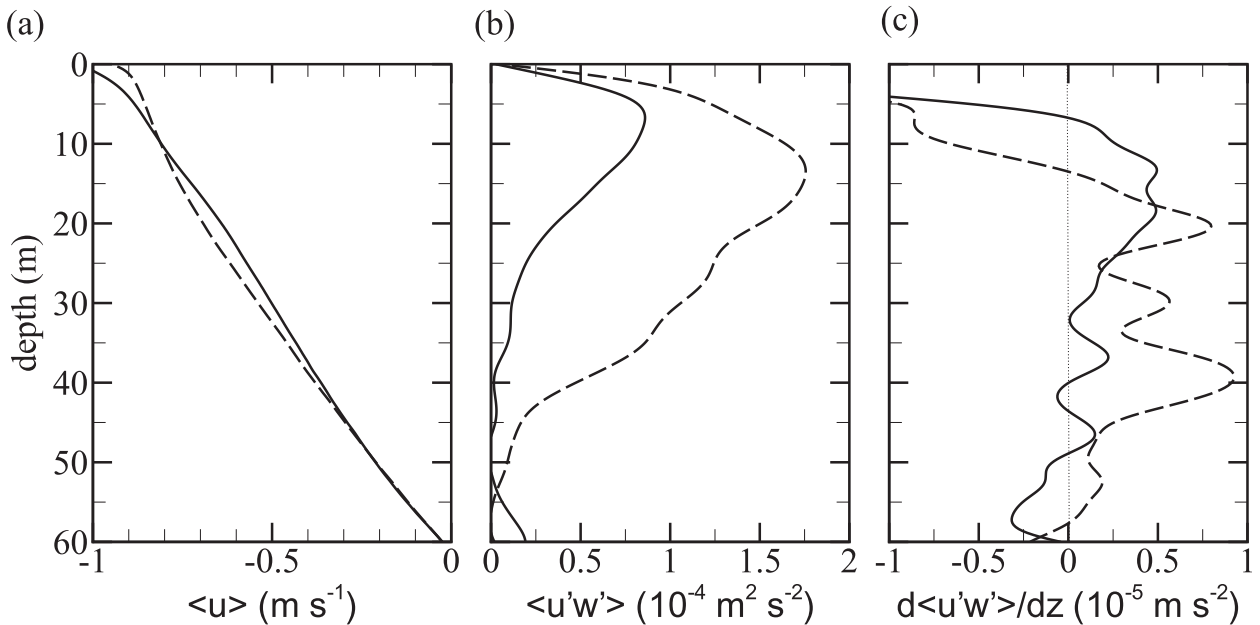
FIG. 9. Horizontally averaged profiles of (a) $\langle u \rangle$, (b) $\langle u'w' \rangle$, and (c) its vertical divergence at 1800 (solid) and 2000 LT (dashed) during the third night. As the wind stress generates turbulence in the surface layer, the divergence of the Reynolds stress increases to larger positive values in the region between depths of 20 and 50 m. This causes the acceleration on the left-hand side of Eq. (10) to become negative. The zonal flow in this region accelerates in the westward direction, that is, $\langle u \rangle$ becomes more negative. The westward acceleration increases the shear rate in this region as was shown in Fig. 8a.

7. Conclusions

Using an LES model of an EUC at oceanographic scale, we have investigated the dynamics leading to occurrence of the deep-cycle turbulence. The model assumes an initial background condition that is suggested by the observational data. A steady wind stress and a diurnal buoyancy flux are applied at the surface for a three-night period. Bursts of elevated dissipation rate are seen to occur preferentially at nighttime, between 1800 and 0600 LT, and at depths well below the surface convective layer. The bursts are preceded by near-N oscillations in the isopycnals. The characteristics of the oscillations and the dissipation agree with observational data. The oscillations propagate westward and have a near-N frequency of 0.004–0.005 Hz and a wavelength of 314–960 m. The magnitude of the enhanced dissipation rate is up to three orders of magnitude larger than the daytime value at the same depth.

While there are different hypotheses regarding the pathway leading to deep-cycle turbulence, analysis of recent observations suggests the following process. First, the background condition of the EUC intermittently becomes unstable; then a shear instability grows leading to the development of near-N oscillations. Finally, the instability develops nonlinearly into turbulence, presumably as in a K–H shear instability event (Moum et al. 2011; Smyth et al. 2013). The results from our simulation

broadly support this hypothesis, not the alternative hypothesis of propagating internal waves that overturn. The results further add to the present understanding of the route to turbulence with the following points:

(i) The background condition in the EUC region, as a result of turbulent mixing, tends to be marginally stable with the gradient Richardson number clustering between 0.2–0.3. Shear instability develops at the base of the surface layer when Ri_g falls below 0.2.

(ii) The growth of shear instability and subsurface turbulence is linked to the diurnal variability in the surface heating. During each 24-h period, deep-cycle turbulence commences with a region of stratified shear with Ri_g less than 0.2 that forms below the surface mixed layer in the early evening. K–H-like billows form and interact with the preexisting EUC shear to form downward-penetrating, sheared vortical structures. The sheared region moves downward to 90-m depth and turbulent patches continue throughout the night. These LES results agree well with the observation of a descending shear layer and concomitant turbulence by Smyth et al. (2013) that has recently become available.

(iii) The downward turbulent momentum flux, that is, Reynolds stress, is found to be key to the nighttime events of shear instability. When the surface layer exhibits active turbulence from the wind stress in the

early evening, the vertical divergence of the Reynolds stress enhances the shear rate in the region below.

(iv) The near-N oscillations are related to the evolution of a Holmboe instability wave.

In our previous study (Pham et al. 2012), we have performed a direct numerical simulation of an EUC flow assuming a background condition in which a Holmboe shear instability can develop at the base of the surface layer. In that study, we focused on the evolutionary process in which the shear instability can generate deep-cycle turbulence at depths greater than where it initially develops. We found the near-N oscillations to be associated with a traveling Holmboe wave, and the growth of the Holmboe shear instability, secondary K–H-like shear instability, and downward vortex penetrations to cause turbulence at depth. In the present study, we are able to identify how the surface forcing, that is, the wind stress and buoyancy flux, can drive the EUC system to the unstable condition that we assume in our previous study. As discussed, the diurnal cycle of surface buoyancy flux is key to the increase in shear and the decrease of Ri$_g$ to below 0.2 at the base of the surface mixed layer. Shear instabilities and turbulence ensue as in the previous DNS. However, unlike the previous DNS, the initial instability growth is not dominated by the Holmboe mode but rather we see a mixture of instabilities that cannot be clearly identified as either Holmboe or K–H. The later nighttime turbulence in the LES model is due to overturning K–H billows and downward penetration of stretched vortical structures, similar to turbulence in the prior DNS.

While our simulation is able to capture the dynamical process leading to deep-cycle turbulence, we have excluded many other processes that also can trigger shear instability. For example, a sudden wind burst can create active turbulence in surface layer, and thereby, trigger shear instability in the EUC. Similarly, Langmuir turbulence can also generate the vertical divergence of Reynolds stress and enhance shear at the base of surface layer. In these scenarios, shear instability could be triggered even during daytime.

REFERENCES

Carpenter, J. R., G. A. Lawrence, and W. D. Smyth, 2007: Evolution and mixing of asymmetric Holmboe instabilities. *J. Fluid Mech.,* **582,** 103–132.

Gregg, M. C., H. Peters, J. C. Wesson, N. S. Oakey, and T. J. Shay, 1985: Intensive measurements of turbulence and shear in the Equatorial Undercurrent. *Nature,* **314,** 140–144.

Hebert, D., J. Moum, C. Paulson, and D. Caldwell, 1992: Turbulence and internal waves at the equator. Part II: Details of a single event. *J. Phys. Oceanogr.,* **22,** 1346–1356.

Holmboe, J., 1962: On the behaviour of symmetric waves in stratified shear layers. *Geofys. Publ.,* **24,** 67–112.

Jacobitz, F. G., S. Sarkar, and C. W. VanAtta, 1997: Direct numerical simulations of the turbulence evolution in a uniformly sheared and stably stratified flow. *J. Fluid Mech.,* **342,** 231–261.

Lien, R.-C., M. McPhaden, and M. Gregg, 1996: High-frequency internal waves at 0°, 140°W and their possible relationship to deep-cycle turbulence. *J. Phys. Oceanogr.,* **26,** 581–600.

——, E. D'Asaro, and M. McPhaden, 2002: Internal waves and turbulence in the upper central equatorial Pacific: Lagrangian and Eulerian observations. *J. Phys. Oceanogr.,* **32,** 2619–2639.

McPhaden, M., and H. Peters, 1992: Diurnal cycle of internal wave variability in the equatorial Pacific Ocean: Results from moored observations. *J. Phys. Oceanogr.,* **22,** 1317–1329.

Moum, J. N., D. Hebert, C. Paulson, and D. Caldwell, 1992: Turbulence and internal waves at the equator. Part I: Statistics from towed thermistors and a microstructure profiler. *J. Phys. Oceanogr.,* **22,** 1330–1345.

——, J. D. Nash, and W. D. Smyth, 2011: Narrowband oscillations in the upper-equatorial ocean. Part I: Interpretation as shear instabilities. *J. Phys. Oceanogr.,* **41,** 397–410.

Peters, H., M. Gregg, and T. Sanford, 1994: The diurnal cycle of the upper-equatorial ocean: Turbulence, fine-scale shear, and mean shear. *J. Geophys. Res.,* **99** (C4), 7707–7723.

Pham, H. T., and S. Sarkar, 2010: Internal waves and turbulence in a stable stratified jet. *J. Fluid Mech.,* **648,** 297–324.

——, ——, and K. B. Winters, 2012: Near-N oscillations and deep-cycle turbulence in an upper Equatorial Undercurrent model. *J. Phys. Oceanogr.,* **42,** 2169–2184.

Skyllingstad, E., and D. Denbo, 1994: The role of internal gravity waves in the equatorial current system. *J. Phys. Oceanogr.,* **24,** 2093–2110.

Smyth, W. D., and W. R. Peltier, 1989: The transition between Kelvin–Helmholtz and Holmboe instability: An investigation of the overreflection hypothesis. *J. Atmos. Sci.,* **46,** 3698–3720.

——, J. N. Moum, and D. R. Caldwell, 2001: The efficiency of mixing in turbulent patches: Inferences from direct simulations and microstructure observations. *J. Phys. Oceanogr.,* **31,** 1969–1992.

——, ——, and J. D. Nash, 2011: Narrowband oscillations at the upper equatorial ocean. Part II: Properties of shear instabilities. *J. Phys. Oceanogr.,* **41,** 412–428.

——, ——, L. Li, and S. A. Thorpe, 2013: Diurnal shear instability, the descent of the surface shear layer, and the deep cycle of equatorial turbulence. *J. Phys. Oceanogr.,* in press.

Wang, D., and P. Muller, 2002: Effects of equatorial undercurrent shear on upper-ocean mixing and internal waves. *J. Phys. Oceanogr.,* **32,** 1041–1057.

——, J. McWiliams, and W. Large, 1998: Large-eddy simulation of the diurnal cycle of deep equatorial turbulence. *J. Phys. Oceanogr.,* **28,** 129–148.

Wijesekera, H., and T. Dillon, 1991: Internal waves and mixing in the upper-equatorial Pacific Ocean. *J. Geophys. Res.,* **96** (C4), 7115–7125.